Environ. Eng. Res. 2023; 28(1): 210569
https://doi.org/10.4491/eer.2021.569

pISSN 1226-1025
eISSN 2005-968X

Research

Amino-modified Mg-MOF-74: Synthesis, characterization and CO_2 adsorption performance

Xiaoying Lin†, Weipeng Zeng, Minyi Liu, Qinhua Zhong, Ting Su, Linzhu Gong, Yamin Liu

School of Ecological Environment and Urban Construction, Fujian University of Technology, Fuzhou 350018 P.R.China

Received November 15, 2021 **Revised** January 07, 2022 **Accepted** February 03, 2022

ABSTRACT

Based on the solvothermal method to synthesize Mg-MOF-74, the *amino*-functionalized Mg-MOF-nNH_2 was prepared through addition of amino-containing ligands. Physicochemical properties of Mg-MOF-nNH_2 materials were well characterized by Powder X-ray diffraction (PXRD), Scanning electron microscope (SEM), Fourier transform infrared spectroscopy (FT-IR), N_2 adsorption/desorption isotherms (BET). The adsorption properties of the resulting materials were studied for CO_2. In all the samples, the micropore volume of Mg-MOF-1/8NH_2 was 0.46 $cm^3\,g^{-1}$ and the specific surface area was 924.19$m^2\,g^{-1}$, the highest CO_2 saturated adsorption capacity was 3.9 mmol g^{-1}, and the dynamic adsorption capacity was 1.27 mmol g^{-1}. The adsorption processes agreed well with the Langmuir isotherm and Avrami model.

Keywords: Adsorption, Amino-functionalization, Carbon dioxide, Metal organic frameworks

1. Introduction

Global warming has become increasingly serious and environmental problems such as rising sea levels, floods and frequent ocean storms caused by climate change have become increasingly prominent [1]. Burning of fossil fuels such as coal and petroleum, oil refining, steel smelting and other chemical industry are the main activity that emits CO_2 to the atmosphere [2]. In order to minimize CO_2 emissions, the most effective method available for control the increasing concentration of carbon dioxide in the atmosphere is carbon capture and sequestration (CCS) [3]. Metal-organic frameworks (MOFs) can be used as an adsorbent in the adsorption of carbon dioxide and have shown better performance compared to traditional adsorbents such as zeolite, mesoporous silica and activated carbon. Currently, several MOFs materials have been used in the adsorption of carbon dioxide research, such as Mg-MOF-74 [4], MIL-101(Cr) [5], Cu-BTC [6], MIL-53(Al) [7], UiO-66(Zr) [8], and so on. Of these, Mg-MOF-74 has a broad prospect of adsorption of carbon dioxide application due to their unique structural characteristics, large surface areas and enriched unsaturated metal sites [9]. However, the adsorption interaction between the Mg-MOF-74 and the carbon dioxide molecules is a weak physical action, and it is suitable for applicable to low temperature and low pressures environment, which has largely restricted their practical applications. Therefore, it is of great significance to enhance the force between the Mg-MOF-74 and the carbon dioxide molecules in order to increase the adsorption capacity of the material at a higher temperature [10].

It is found that the presence of nitrogen-containing functional groups can enhance the CO_2 adsorption capacity of MOFs. The Lewis basic site provided by the nitrogen-containing group has a strong affinity with CO_2 as a conjugated base. Presently, most of the modifications of basic groups are reported about post-synthetic modification. For example, loading nitrogen-containing groups in MOFs pore canals by impregnating with various alkaline nitrogen-containing substances [11], grafting nitrogen-containing groups after the material's synthesis [12]. Although these post-synthetic modification methods can increase the affinity of the materials to carbon dioxide molecules, the introduction of nitrogen-containing groups will block the original microporous structure of the materials and reduce the specific surface area of the materials, resulting in a decrease in physical adsorption capacity. The direct synthesis of functionalized MOFs materials from the connectors

† Corresponding author
E-mail: linxy@fjut.edu.cn
Tel: +86 13509322330
ORCID: 0000-0002-2193-8490

containing amino or nitrogen heterocycles can not only maintain the original topological structure of the materials, have a large specific surface area, but also enhance CO_2 affinity, so it is an excellent alternative [13].

Adsorbent regeneration procedure is very important in the CO_2 adsorption process. The energy required for adsorbents regeneration is a key factor to evaluating the economic feasibility of the adsorption process. The regeneration process of the adsorbent is usually achieved by changing the pressure (under lower pressure) and/or temperature (higher temperature) to release the adsorbed CO_2. The difference between adsorption conditions and regeneration conditions will determine the working capacity of the adsorbent. A variety of techniques have been tried for the regeneration of adsorbents [14], including: (1) pressure swing adsorption (PSA), (2) vacuum swing adsorption (VSA), (3) temperature swing adsorption (TSA), (4) Electrical swing adsorption (ESA), (5) hybrid regeneration approaches, such as: pressure-temperature swing adsorption (PTSA) and steam aided vacuum swing [15]. Both PSA and VSA are performed by changing the pressure, In PSA, adsorption is carried out under higher than atmospheric pressure, and desorption is conducted under atmospheric pressure; in VSA, adsorption is carried out under atmospheric pressure, and desorption is conducted under lower pressure [16]. Relative to PSA and VSA, TSA can be directly thermally driven. In TSA, adsorbent regeneration can be realized by hot air and water vapor, the regeneration time is usually longer than that of PSA due to thermal inertia. In order to overcome the inconvenience of using hot air, a heating process by the Joule effect is proposed, this is Electrical swing adsorption (ESA). Compared with PSA and TSA, ESA has some advantages, including require less heat, faster heating rate, better desorption kinetics, independent air flow and heat source control system [17].

To summarize, in this work, functionalized Mg-MOF-74 was synthesized by adding amino-containing ligands. the 2,5-dihydroxyterephthalic acid and 2-amino terephthalic acid were used as the ligands material, Mg $(NO_3)_2{\cdot}6H_2O$ was used as a metal center ion donor, the mixed solution of *N, N*-dimethylformamide (DMF), distilled water and ethanol were used as the solvent, to synthesize Mg-MOF-nNH_2 and the carbon dioxide adsorption capacity of synthetic materials was measured, and look forward to its application prospect.

2. Experimental

2.1. Materials

Magnesium nitrate hexahydrate (Mg $(NO_3)_2{\cdot}6H_2O$) (≥ 98%, Sinopharm), *N, N*–dimethylformamide (DMF) (≥ 99%, Sinopharm), 2,5-dihydroxyterephthalic acid ($C_8H_6O_6$) (≥ 99%, Aladdin), 2-amino-terephthalic acid($C_8H_7NO_4$) (≥ 99%, Aladdin), methanol (CH_4O) (≥ 99.5%, Sinopharm),anhydrous ethanol(C_2H_6O) (≥ 99.5%, Sinopharm), carbon dioxide(CO_2) (≥ 99.999%, Fuzhou Xinhang Gas Co., Ltd.), nitrogen(N_2) (≥ 99.999%, Fuzhou Xinhang Gas Co., Ltd.).

2.2. Preparation of Materials

Synthesis of Mg-MOF-74: The typical synthetic process was performed as follows: Mg $(NO_3)_2{\cdot}6H_2O$ (1.95 mmol, 0.712 g) and 2,5-dihydroxyterephthalic acid (0.83 mmol, 0.167 g) were dissolved in the mixed solution of *N, N*-Dimethylformamide (DMF), 67.5 mL deionized water 4.5 mL, ethanol 4.5 mL (*V*(DMF):*V*(H_2O):*V*(CH_3CH_2OH) = 15:1:1). After ultrasound was used for 30 min, the solution was transferred into a Teflon-lined autoclave (100 mL) and kept at 398K for 24 h. Next, the sample was cooled naturally to room temperature, the precipitate was filtered and the product was immersed in methanol for 3 d, the supernatant solution was changed every 12 h, then the solid product was separated by centrifugation. Finally, the product was placed in a vacuum drying box and dried for 12 h at 373K, dark yellow solid was obtained. The samples were designated as Mg-MOF-74.

Synthesis of Mg-MOF-nNH_2: The Mg $(NO_3)_2{\cdot}6H_2O$ (1.95 mmol, 0.712 g), 2,5-dihydroxyterephthalic acid (x mmol), 2-amino-terephthalic acid (y mmol) were weighed (where x: y = 10:1, 8:1, 6:1, 4:1), dissolved in the mixed solution of *N, N*-dimethylformamide (DMF) ,67.5mL deionized water 4.5 mL, ethanol 4.5 mL (*V*(DMF):*V*(H_2O):*V*(CH_3CH_2OH) = 15:1:1). The next steps were the same as for the synthesis of Mg-MOF-74. the samples are designated as Mg-MOF-nNH_2. (n = y/x)

2.3. Characterization

Structural analysis was carried out by powder Xray diffraction (PXRD, Ultima IV, Buker, Germany). The Fourier infrared analysis was carried out by Fourier transforming infrared spectrometry (FTIR, SP2000, Thermo Nicolet Corporation, USA). The surface morphology of the samples was observed using a scanning electron microscope (SEM, Hitachi SU8010, Hitachi High Technologies Corp, Japan). The thermal stability of the samples was determined by Thermogravimetric Analysis (TG, TG209F3, Netzsch, Germany) The specific surface area and the pore size of samples were determined by an automatic surface area and pore size analyzer (AutosorbiQ2, Quantachrome Instruments Co., USA).

2.4. Adsorption Experiments

2.4.1. Static Adsorption

The static adsorption-desorption experiment of CO_2 was carried out by using a thermogravimetric analyzer (TG209-F3, Netzsch, Germany). The sample was heated and degassed to constant weight in high purity N_2 flow (40 cm^3/min), and introduction of high purity CO_2/N_2 mixture for 1 h after the system temperature dropped to test temperature, recorded sample weight. Next, the gas in the system was converted into a high purity N_2 flow, and the temperature was raised to 373k and kept for 1 h. After desorption was completed, the temperature was set to the next adsorption temperature, and the next adsorption process continued. The adsorption capacity q_a is calculated using Eq. (1).

$$q_a = \frac{1000(m_e - m_0)}{44m_0} \quad (1)$$

Where q_a (mmol/g) is the adsorption capacity; m_e (mg) is the weight at the end of adsorption; m_0 (mg) is the initial sample weight; 44 is the molecular weight of CO_2.

2.4.2. Adsorption kinetic analysis

Lagergren pseudo first-order kinetic model [18], Ho pseudo second-order kinetic model [19] and Avrami fractional order dynamics model [20] were used to explore the adsorption mechanism. The expression of the Lagergren pseudo first-order adsorption kinetic model is as follows Eq. (2):

$$\frac{dq_t}{dt} = k_1\left(q_e - q_t\right) \tag{2}$$

where q_t (mmol/g) is the adsorption capacity at the time t; q_e (mmol/g) is saturated adsorption capacity; k_1 (mmol·g^{-1}·s^{-1}) is the quasi-first-order adsorption rate constant.

The integral form of Eq. (2) is

$$q_t = q_e\left(1 - e^{-k_1 t}\right) \tag{3}$$

The Ho pseudo-second-order adsorption kinetic model can be written as below in Eq. (4)

$$\frac{dq_t}{dt} = k_2\left(q_e - q_t\right)^2 \tag{4}$$

where k_1 (mmol·g^{-1}·s^{-1}) is the quasi-second-order adsorption rate constant.

The integral form of Eq. (5) is

$$q_t = \frac{t}{\frac{1}{k_2 q_e^2} + \frac{t}{q_e}} \tag{5}$$

The Avrami fractional-order dynamics expressions such as Eq. (6)

$$\frac{dq_t}{dt} = k_a^n t^{n-1}\left(q_e - q_t\right) \tag{6}$$

In the equations above, k_a (min^{-1}) is the Avrami model kinetic constant; n is the Avrami index, dimensionless constant; q_e (mmol/g) is the saturated adsorption capacity; q_t (mmol/g) is the adsorption capacity at the time t.

The integral form of Eq. (7) is

$$q_t = q_e\left[1 - e^{-(k_a t)n}\right] \tag{7}$$

2.4.3. Adsorption isotherms analysis

Langmuir and Freundlich models [21, 22] were used to analyze and fit the sorption isotherm data, the linear form of the Langmuir is as follows in Eq. (8):

$$q_e = q_m \frac{K_L P}{1 + K_L P} \tag{8}$$

where q_m (mmol/g) is the maximum adsorption capacity of the Langmuir model; K_L is the Langmuir model constant; p is the CO_2 partial pressure; q_e (mmol/g) is the adsorption capacity at equilibrium.

The linear form of the Freundlich is as follows in Eq. (9):

$$q_e = K_f P^{1/n} \tag{9}$$

where K_f is the Freundlich model constant; n is a nonuniformity factor; p is the CO_2 partial pressure; q_e (mmol/g) is the adsorption capacity at equilibrium.

2.4.4. Adsorption thermodynamics analysis

Thermodynamic parameters were calculated using the following equations [23]:

$$\ln K_L = \left(\frac{\Delta S^0}{R}\right) - \left(\frac{\Delta H^0}{RT}\right) \tag{10}$$

$$\Delta G^0 = \Delta H^0 - T\Delta S^0 \tag{11}$$

where ΔS^0 is the entropy change; ΔH^0 is the enthalpy change; ΔG^0 is the Gibbs free energy change.

Isosteric heats of adsorption were estimated by the Clausius–Clapeyron equation [24], the expression is as follows:

$$\ln\left(p\right) = -\frac{Q_{st}}{RT} + C \tag{12}$$

where ΔH is the equivalent adsorption heat; T (K) is the adsorption temperature.

2.4.5. Breakthrough performance test

CO_2 dynamic adsorption experiments were carried out at atmospheric pressure and different temperatures (303K, 313K, 323K). The experimental setup is shown in Fig. S1. The size of the adsorption column is D × L = 13 × 100 mm, the loading capacity of the adsorbent was 1,000 mg, the outlet CO_2 concentration was detected by gas chromatography (GC9790, Zhejiang Fuli analysis instrument Co., Ltd., China). The working conditions of the instrument included the injector temperature was maintained at 423K, detection temperature was 423K and the temperature of the chromatographic column was 423K. Helium was used as the carrier gas. The continuous injection method was used to detect the gas concentration at the outlet once per 1.5 min.

The adsorption breakthrough curve is the variation curve of outlet gas concentration with time and the position where the concentration of gas at the outlet rises sharply is the breakthrough point, corresponding time t_1 is the adsorption penetration time [25]. In this paper, the saturated adsorption capacity of adsorbent for CO_2 is calculated based on the adsorption breakthrough curve and the formula is as follows:

$$q = \frac{1}{M} \times \left[\int_0^t Q \times \frac{C_0 - C}{1 - C}\, dt\right] \times \frac{T_0}{T} \times \frac{1}{V_m} \tag{13}$$

where q (mmol/g) is the adsorption capacity; Q (cm^3/min^{-1}) is the gas flow rate; C_0 (%) is the inlet concentration of CO_2; C (%) is

the outlet concentration of CO_2; T (K) is the adsorption temperature; T_0 is 273K; M (mg) is the mass of adsorbent; V_m is the molar volume of gas, 22.4 cm^3/min.

According to the model of gas-solid reaction proposed by Yasyeli et al. [26] and the isothermal mass conservation equation of CO_2 concentration in the adsorption column is shown in the following Eq. (14):

$$-Q\frac{dC}{dM}-k_0C\alpha=0 \tag{14}$$

where k_0($m^3 \cdot kg^{-1} \cdot min^{-1}$)is the initial adsorption rate constant; α is the rate of change of the solid reactants activity; α can be expressed by the following Eq. (15):

$$-\frac{d\alpha}{dt}=k_dC^j\alpha^m \tag{15}$$

The unit of k_d is min^{-1}; j indicates the independence of gas adsorption; m means gas adsorption and put-in activity; j = 1, m = 1, the modified form of the breakthrough curve model is as follows:

$$\frac{C}{C_0}=\exp\left[\frac{\left[1-\left(\exp\left(\frac{k_0M}{Q}\left(1-\exp\left(-k_dt\right)\right)\right)\right)\right]}{1-\exp\left(-k_dt\right)}\exp\left(-k_dt\right)\right] \tag{16}$$

Avrami fractional-order dynamics can be used to simulate the adsorption process, the formula is as follows:

$$y=1-e^{-(k_at)^n} \tag{17}$$

where y (%) is desorption ratio; k_a (min^{-1}) is desorption kinetic constant; n is Avrami desorption index, dimensionless constants.

3. Results and Discussion

3.1. Characterization Results

3.1.1. XRD characterization

The XRD patterns of the Mg-MOF-74 and Mg-MOF-nNH_2 are shown in Fig. 1(a). From the figure, the XRD spectra of all samples exhibit two obvious diffraction peaks appeared at 6.9° and 11.9°. The diffraction peak intensity at the 2θ = 11.9° of Mg-MOF-nNH_2 is weaker than Mg-MOF-74, and this indicates that the addition of amino ligands affects the crystallinity of materials [27, 28] A new sharp diffraction peak appears at 2θ = 9.7°, it shows that the addition of amino ligand changes the original crystal structure. When adding a small amount of aminoligands, a small amount of -NH_2 can promote the ionization of -COOH and the probability of coordination between magnesium ion and carboxyl group was increased, this is the reason that the diffraction peak intensity of Mg-MOF-1/10NH_2 and Mg-MOF-1/8NH_2 are sharper than other samples. However, excessive content of -NH_2 causes steric hindrance effect which hinders the coordination of magnesium ions with ligands.

3.1.2. FT-IR analysis

The FT-IR spectrums of Mg-MOF-74 and Mg-MOF-nNH_2 are presented in Fig. 1(b). Peaks at 3,500cm^{-1} and 3,200cm^{-1} are the O-H stretching vibration. The peak of Mg-MOF-nNH_2 here is slightly sharper than that of Mg-MOF-74. It is attributed to the superposition of vibration of -NH_2 which from newly added ligands and stretching vibration of O-H [29].

3.1.3. TG analysis

Thermogravimetric analysis (TGA) weight loss curves are presented in Fig. 2. The slight weight loss at 423K is due to the removal of moisture and residual solvents inside the channel. There is an obvious weight loss in 673K~773K, and the material structure collapses gradually. When the temperature reaches about 903K, with a weight loss of about 50 wt.%. At this time, the coordination bond has been completely broken, the organic ligand is volatilized, and the structure collapses [30]. From Mg-MOF-1/10NH_2 to

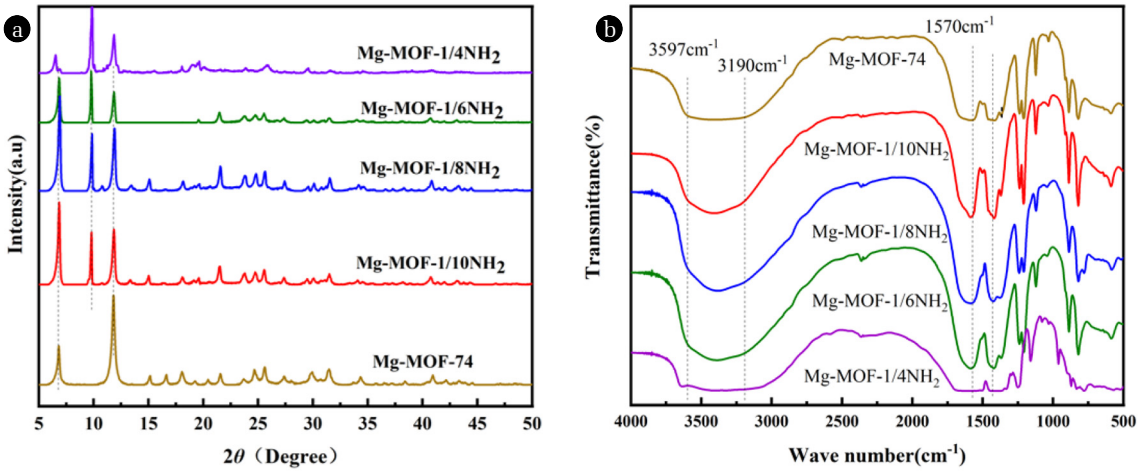

Fig. 1. (a) XRD patterns of Mg-MOF-74 and Mg-MOF-nNH_2, (b) FT-IR spectrum of Mg-MOF-74 and Mg-MOF-nNH_2.

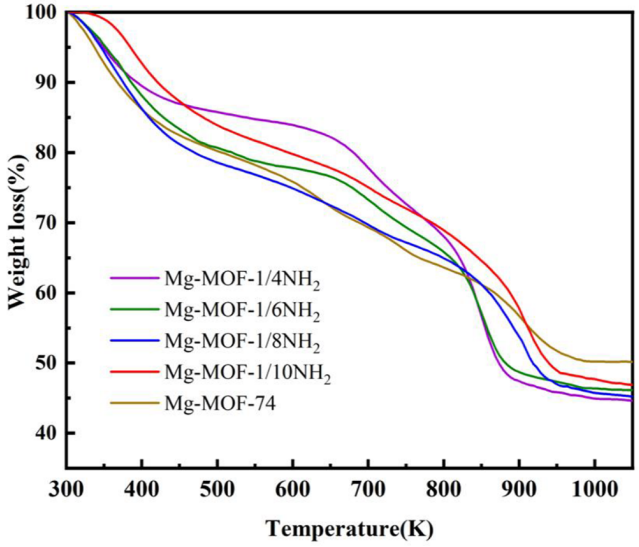

Fig. 2. TGA curve of Mg-MOF-74 and Mg-MOF-nNH$_2$.

Mg-MOF-1/4NH$_2$, the equilibrium point gradually shifts to the left, and the thermal stability decreases.

3.1.4. N_2 adsorption/desorption isotherm

N_2 adsorption/desorption isotherms and pore size distributions of the samples are depicted in Fig. 3. Typical Type-IV isotherms are found in the Mg-MOF-nNH$_2$, demonstrating that the material obvious mesoporous structure. With the increase of the amount of 2-aminoterephthalic acid, the specific surface area of Mg-MOF-nNH$_2$ decreased gradually. It may be due to the competitive coordination between 2-aminoterephthalic acid ligand and 2.5 dihydroxyterephthalic acid, and excessive -NH$_2$ makes the crystal produce defects and increase pore size [31].

Table S1 shows the parameters of pore structure. Compared with Mg-MOF-74, the specific surface area of Mg-MOF-1/8NH$_2$ decreased 198m^2/g, but the proportion of micropore volume increased, and the specific surface areas of Mg-MOF-1/6NH$_2$ and Mg-MOF-1/4NH$_2$ are reduced by about 430m^2/g and 607m^2/g, respectively. The specific surface area has great impact on the adsorption properties of adsorbent material. Therefore, Mg-MOF-1/8NH$_2$ was selected to further study its CO_2 adsorption properties.

3.1.5. SEM analysis

Fig. 4 shows SEM images and EDS spectrums of Mg-MOF-74 and Mg-MOF-1/8NH$_2$. The crystal of Mg-MOF-74 is mainly composed of two kinds of morphology, one is cone-shaped needle shape, the other is cauliflower-like morphology bonded by short columnar grains, and the crystal surface is smooth. The result is consistent with reports in the literature [32]. Compared with Mg-MOF-74, Mg-MOF-1/8NH$_2$ crystal has a certain thickness, single crystal is the hexagonal pyramid and exhibites a rough and uneven surface, indicating that the addition of new ligands changes the morphology and structure of the materials. The content of the N element in Mg-MOF-1/8NH$_2$ was 0.25% determined by EDS, indicating that the amino ligand successfully entered the crystal structure.

3.2. Studying the Adsorption Performance

3.2.1. Adsorption kinetics analysis

Fig. 5(a) shows the adsorption kinetics curve of sample Mg-MOF-1/8NH$_2$. During the initial stage of adsorption, the material is rich in active sites and binds to CO_2 rapidly, and the adsorption rate is faster. With the decrease of active sites, the adsorption rate decreases, and the adsorption capacity increases slowly until the adsorption equilibrium. The adsorption capacity decreases with the increase of temperature, due to the adsorption process is an exothermic process, it shows that the adsorption process is mainly determined by the temperature [33]. The results of various adsorption parameters obtained from the kinetic models are presented in Table S2. At 323K, the R^2 value of the pseudo-second-order kinetic model is the largest (R^2 = 0.991). The adsorption at higher temperatures is suitable to be fitted by the pseudo-second-order kinetic model, and chemical adsorption plays an important role. The correlation coefficient R^2 fitted by the Avrami model is 0.999. The adsorption process of CO_2 on Mg-MOF-1/8NH$_2$ has both physical adsorption and chemical adsorption, which is dominated by chemical adsorption.

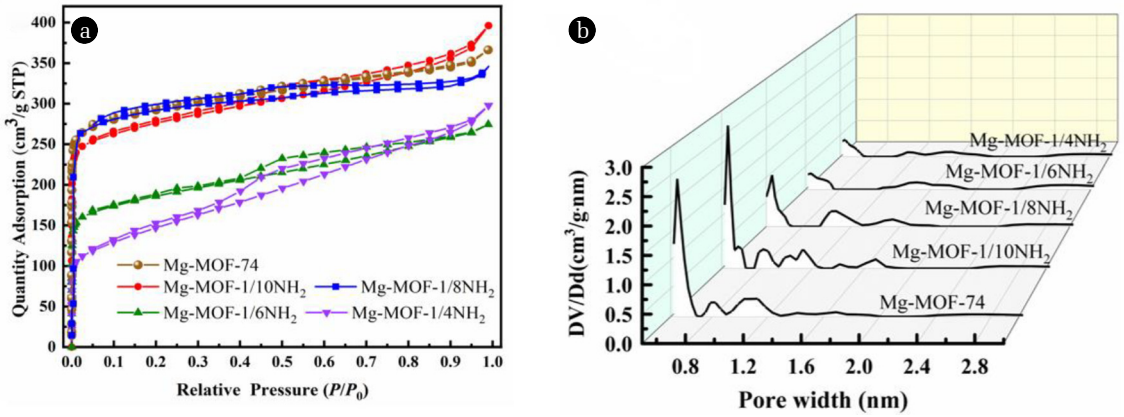

Fig. 3. Nitrogen adsorption/desorption isotherm and pore size distribution of Mg-MOF-74 and Mg-MOF-nNH$_2$: (a) Nitrogen adsorption/desorption isotherm of Mg-MOF-74 and Mg-MOF-nNH$_2$; (b) Pore size distribution of Mg-MOF-74 and Mg-MOF-nNH$_2$.

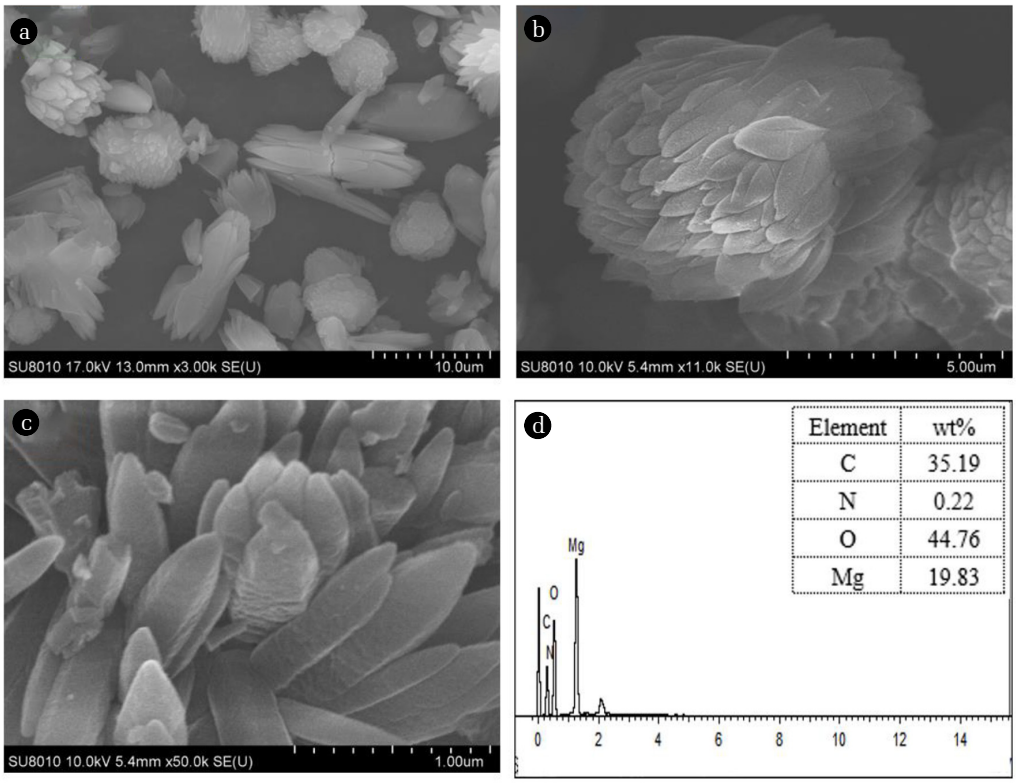

Fig. 4. SEM images and EDS spectrum of Mg-MOF-74 and Mg-MOF-1/8NH_2 :(a) SEM image of Mg-MOF-74; (b), (c) SEM image of Mg-MOF-1/8NH_2; (d) EDS spectrum of Mg-MOF-1/8NH_2.

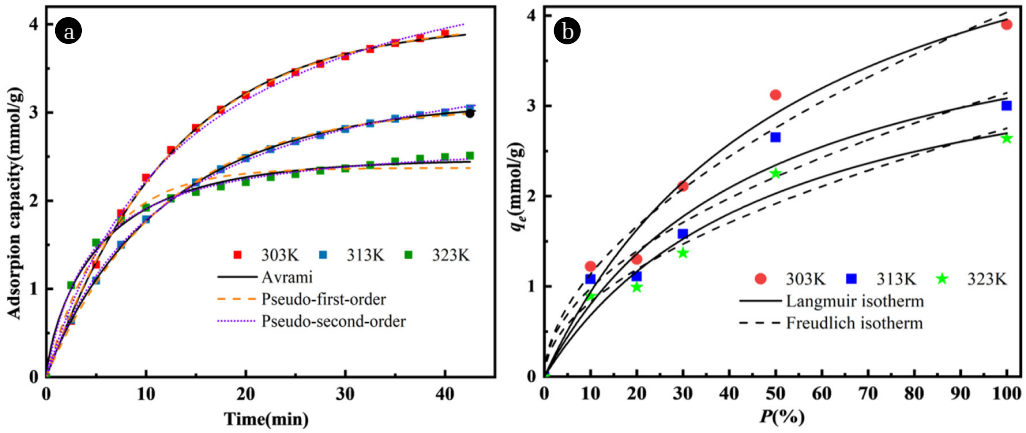

Fig. 5. (a) The curves of adsorption kinetic, (b) The curves of adsorption isotherms.

3.2.2. Adsorption isotherm analysis

Fig. 5(b) shows the results of the isothermal model simulation. With the increase of CO_2 concentration, the adsorption capacity increases, and the CO_2 adsorption properties of the materials are better in the lower temperature range. As the results in Table S3, the R^2 obtained by fitting the data with the Langmuir equation is larger than that of the Freundlich equation, and the adsorption process is more fitted the Langmuir model. $1/n < 1$ indicates that adsorption is easy to proceed.

Table S4 shows the comparison of the saturated adsorption capacity of CO_2 between Mg-MOF-74 and Mg-MOF-1/8NH_2 at different temperatures. The binding force between Mg-MOF-74 and adsorbate is weak, and the adsorption capacity decreases with the increase of temperature, due to the CO_2 molecules desorption from adsorbents at high temperatures. The adsorption capacity of Mg-MOF-1/8NH_2 which modified by 2-aminoterephthalic acid increased by 9, 18 and 44% at 303K, 313K and 323K, respectively. It is possible due to the chemical adsorption is increased after

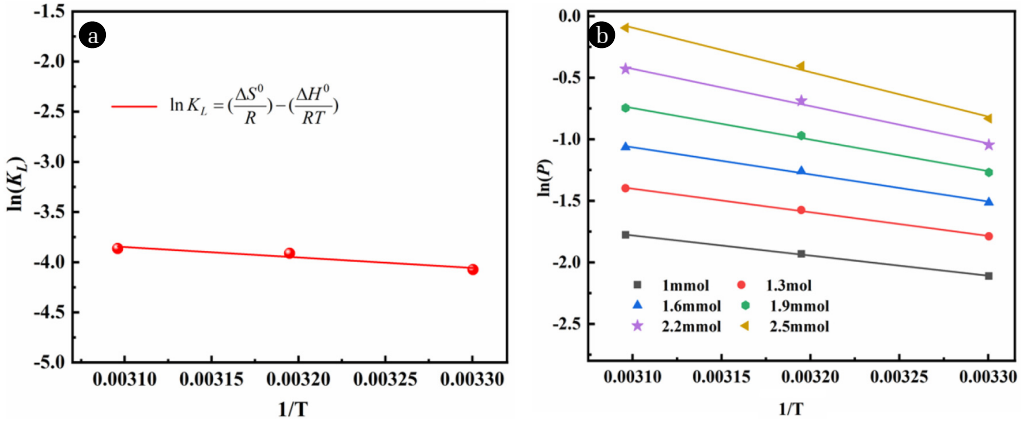

Fig. 6. (a) Van't Hoff plots for estimation of thermodynamic parameters for CO_2 adsorption (b) ln(P) versus 1/T and regression lines at different amounts of adsorbed CO_2.

amino functionalization, and the binding force between CO_2 molecules and adsorbents is stronger.

3.2.3. Adsorption thermodynamics analysis

Fig. 6. shows the Van' Hoff plot of 1/T and ln(P) plot of 1/T at three temperatures. Table S6 shows the results of thermodynamic parameters, and the value of Q_{st} is shown in Table S5. The ΔH value is -8.64 kJ/mol, which shows heat release during the adsorption process, ΔS is 5.2 J/mol suggests a more random contact at the solid/gas, and the affinity of the material to CO_2 is high. The average isovolumetric heat of adsorption is 41.54 kJ/mol, which is slightly higher than the enthalpy of physical adsorption (< 40 kJ/mol). During adsorption, there is both chemical adsorption and physical adsorption, mainly chemical adsorption.

3.2.4. Results of dynamic a Cyclic adsorption performance

The relationship between the adsorption of the CO_2 and the number of cycles after five cycles can be seen in the Fig. 7. After five adsorption and desorption cycles, the fifth adsorption capacity of Mg-MOF-1/8NH_2 still retains 77% of that of the first adsorption, indicating that Mg-MOF-1/8NH_2 has a good regeneration ability.

3.2.5. Results of dynamic adsorption

Fig. 8 (a), (b) shows the breakthrough curve of different temperatures of Mg-MOF-74 and Mg-MOF-1/8NH_2 at CO_2 concentration of 10%, and Table S7 and Table S8 show the corresponding parameters of the model of Mg-MOF-74 and Mg-MOF-1/8NH_2. As the figure shows that the breakthrough time decreases with the increase of adsorption temperature. At 303K, the breakthrough curves of Mg-MOF-1/8NH_2 reached the breakthrough point at 4min, and the breakthrough point and adsorption saturation point of Mg-MOF-1/8NH_2 at 313K and 323K are delayed compared with the breakthrough point and adsorption saturation point of Mg-MOF-74, indicating that the adsorption capacity of Mg-MOF-1/8NH_2 increased, which showed that the adsorption capacity of Mg-MOF-1/8NH_2 increased, the results are consistent with the results of static adsorption experiments. With the increase of temperature, the diffusion resistance of CO_2 molecules molecules from the surface into the pore of the adsorbent decrease. With the enhanced mobility of CO_2 molecules in the pores, more CO_2

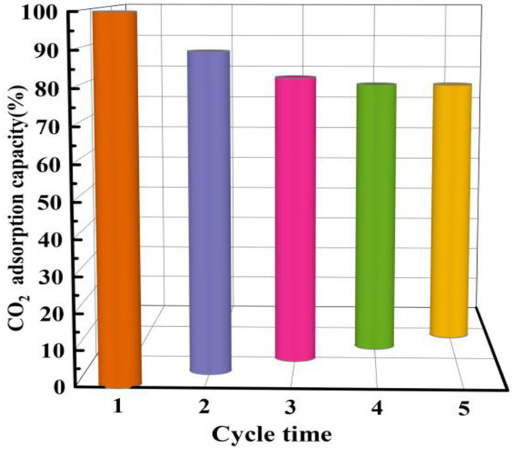

Fig. 7. Cyclic adsorption on Mg-MOF-1/8NH_2.

molecules are fully combined with the active sites resulting in adsorbed by adsorbents. The adsorption process is an exothermic reaction, and low temperature promotes adsorption.

Fig. 8 (c), (d) shows the breakthrough curves of different CO_2 concentrations at 303K and 40 mL/min flow rate of Mg-MOF-74 and Mg-MOF-1/8NH_2. According to the figures, the saturation point gradually delays with the decrease of initial concentration, and the breakthrough curve becomes smooth at the same time. Table S9 and Table S10 show the parameters of the deactivation model obtained by fitting the experimental results of Mg-MOF-74 and Mg-MOF-1/8NH_2. According to the data of tables, the correlation coefficient R^2 is more than 0.9, and the adsorbent activity decreases significantly with the increase of the adsorption degree. The change of the adsorption capacity of adsorbent may correlate with the change of pore structure, specific surface area and active site distribution of the adsorbent changes. The inactivation rate k_d increases with the increase of initial concentration, indicating that the high CO_2 partial pressure promotes the diffusion of CO_2 to the reaction site. The adsorption capacity q increases with the increase of concentration, indicating that high pressure CO_2 promotes the reaction with the adsorbent

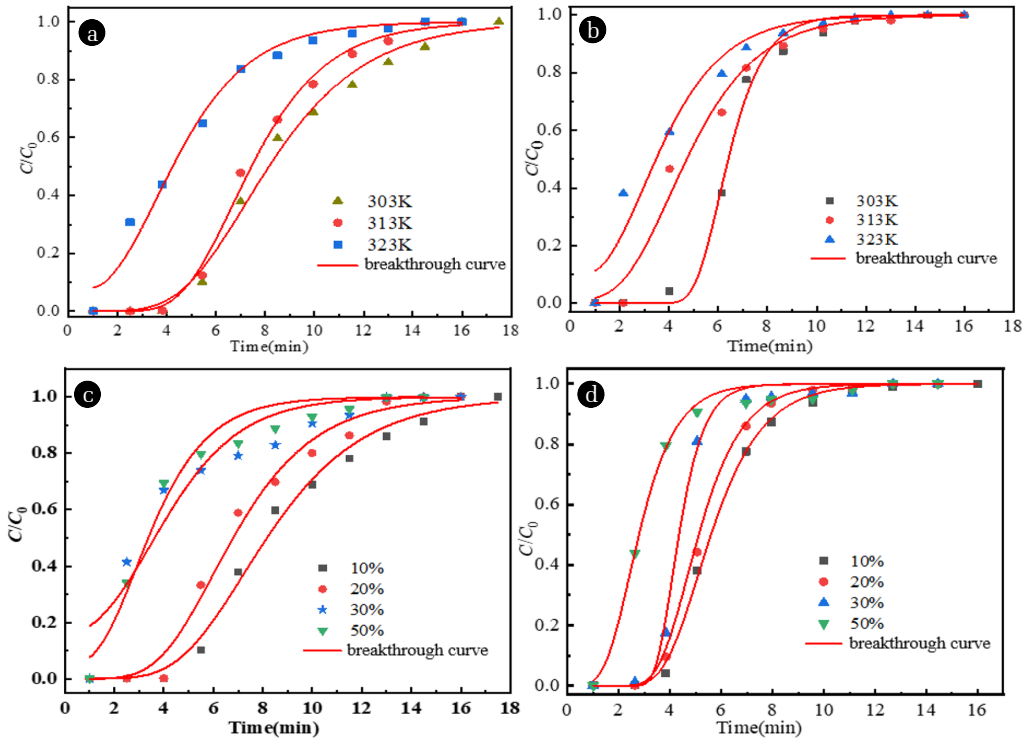

Fig. 8. Breakthrough curves at different temperatures of (a) Mg-MOF-1/8NH_2 (b) Mg-MOF-74, Breakthrough curve of different concentrations of (c) Mg-MOF-1/8NH_2 (d) Mg-MOF-74.

4. Application Prospect

The carbon dioxide adsorption capacity of several common adsorbents are listed in Table S11, and it shows that the material prepared in this work has a high carbon dioxide adsorption capacity at room temperature and normal pressure, which suggests that it is potentially an good sorbent for CO_2. The characterization results confirmed that the high temperature has a certain effect on the structure of the material, and then affects the CO_2 adsorption capacity of materials. So, we suggest that it can be applied to CO_2 capture in confined spaces under room temperature and normal pressure, such as submarines, space station and other environments.

The fine adsorption particles very easy to agglomeration and plugging phenomena in the device in practical applications [34], and then affects the CO_2 adsorption。 To overcome this problem, we suggest that we can mix the prepared adsorbent particles in this paper with the binder to produce the larger-sized adsorbent particles and spherical adsorbent. Cousin-Saint-Remi [35] and this workmates used ZIF-8 mixed with binder polyvinylformal (PVFM) to prepare ZIF-8 beads.The results show that the beads possess excellent mechanical strength almost equivalent to a widely used commercial zeolite material and the adsorption capacities are only reduced in proportion with the binder content compared to the pristine material, indicating no binder intrusion in the ZIF-8 pores. In the regeneration process of the adsorbent, We propose that temperature swing adsorption may be a suitable approache for the prepared adsorbent in this paper, due to that the adsorption process of the material is dominated by chemiadsorption..

5. Conclusions

Mg-MOF-nNH_2 with double ligands were synthesized with magnesium as a metal center and 2,5-dihydroxyterephthalic acid and 2-amino terephthalic acid as ligands. The saturated adsorption capacity of CO_2 was 3.9 mmol/g at 303k for Mg-MOF-1/8NH_2. Compared with Mg-MOF-74, the CO_2 adsorption capacity of Mg-MOF-1/8NH_2 increased by 9, 18 and 44% at 303K, 313K and 323K, respectively. The adsorption process accords with the Langmuir model and Avrami model, and the average isothermal heat of adsorption is 41 kJ/mol. Chemical adsorption and physical adsorption occur in the process of adsorption CO_2, mainly chemical adsorption. The material has good adsorption cycle stability and still retains 77% of the initial adsorption after 5 adsorption and desorption cycles. Compared with Mg-MOF-74, Mg-MOF-1/8NH_2 has better dynamic adsorption performance, and the dynamic adsorption capacity is 1.27 mmol/g at 303k.

Acknowledgments

This work was supported by Natural Science Foundation of Fujian Province of China (2020Y0055), Project in Fuzhou Science and Technology Bureau (2020-PT-144) and The Startup Fund for Scientific Research (GY-Z19168), Fujian University of Technology.

Conflict-of-Interest

The authors declare that they have no conflict of interest.

Author Contributions

Dr. X.L. (Professor) and Dr. M.L. (Assistant Professor) jointly drafted the manuscript. Ms. Q.Z. (M.Sc. Student) and Mr. W.Z. (M.Sc. Student) have done all the experiments. Ms. T.S (M.Sc. Student) did literature survey, revised the manuscript. Dr. Y.L. (Professor) and Dr. L.G. (Professor) reviewed the whole work and provided suggestions for the improvement of the paper. All authors have read and agreed to the published version of the manuscript.

References

1. Wang X, Jiang D, Lang X. Future extreme climate changes linked to global warming intensity. *Sci. Bull*. 2017;62:1673-1680.
2. Liu HR, Liang ZH, Wang SY, et al. Synthesis and characterization of a thermosensitive solid amine biomass adsorbent for carbon dioxide adsorption. *J. Environ. Manage*. 2021;292:112722.
3. Huang QH, Ding J, Huang X, et al. Experimental and computational investigation of CO_2 capture on mix-ligand metal-organic framework UiO-66. *Energy Procedia* 2017;105:4395-4401
4. Sohrabi H, Javanbakht S, Oroojalian F, et al. Nanoscale Metal-organic frameworks: recent developments in synthesis, modifications and bioimaging applications. *Chemosphere* 2021;281: 130717.
5. Wan Y H, Semali B, Andrew P, et al. Comparison of MIL-101(Cr) metal-organic framework and 13X zeolite monoliths for CO2 capture. *Micropor. Mesopor. Mater.* 2020;308:110525.
6. Wu YF, Lv AZ, Zhou X, et al. Tuning secondary building unit of Cu-BTC to simultaneously enhance its CO_2 selective adsorption and stability under moisture. *Chem. Eng. J.* 2019;355:815-821.
7. Soleimanpour A, Farsi M, Keshavarz P, et al. Modification of activated carbon by MIL-53(Al) MOF to develop a composite framework adsorbent for CO_2 capturing. *Environ. Sci. Pollut. R.* 2021;28:37929-37939.
8. Ethiraj J, Albanese DE, Civalleri DB, et al. Carbon dioxide adsorption in amine-functionalized mixed-ligand metal–organic frameworks of UiO-66 topology. *Chem. Sus. Chem*. 2014;224: 85-94.
9. Li B, Wen H M, Cui Y, et al. Emerging multifunctional metal-organic Framework materials. *Adv. Mater*. 2016;28:8819-8860.
10. Deng H, Grunder S, Cordova KE, et al. Large-pore apertures in a series of metal-organic frameworks. *Science* 2012;336: 1018-1023
11. Wang N, Mundstock A, Liu Y, et al. Amine-modified Mg-MOF-74/CPO-27-Mg membrane with enhanced H_2/CO_2 separation. *Chem. Eng. Sci.* 2015;124:27-36.
12. Su X, Bromberg L, Martis, et al. Postsynthetic functionalization of Mg-MOF-74 with tetraethylenepentamine: structural characterization and enhanced CO_2 adsorption. *ACS Appl. Mater. Inter.* 2017;9:11299-11306.
13. Hao L, Qiu Q, Li H. Directional functionalization of MOF-74 analogs via ligand pre-installation. *Chinese J. Chem*. 2016;34:220-224.
14. Olajire AA. CO2 capture and separation technologies for end-of-pipe applications – a review. *Energy* 2010;35:2610-26287.
15. Raganati F, Miccio F, Ammendola P. Adsorption of carbon dioxide for post-combustion capture: a review. *Energ. Fuels* 2021;35:12845-12868.
16. Fisher J, Tanthana J, Chuangf SSC. Oxide-supported tetraethylenepentamine for CO_2 capture. *Environ. Prog. Sust.* 2009;28: 589-598.
17. Dhoke C, Zaabout A, Cloete S, et al. Review on reactor configurations for adsorption-based CO_2 capture. *Ind. Eng. Chem. Res*. 2021;60(10):3779-3798.
18. Tseng RL, Wu FC, Juang RS. Characteristics and applications of the lagergren's first-order equation for adsorption kinetics. *J. Taiwan. Inst. Chem. E* 2010;41:661-669.
19. Simonin JP. On the comparison of pseudo-first order and pseudo-second order rate laws in the modeling of adsorption kinetics. *Chem. Eng. J*. 2016;300:254-263.
20. Avrami M. Kinetics of phase chang. I general theory. *J. Chem. Phys*. 1939;7:1103-1112.
21. Langmuir I. The adsorption of gases on plane surfaces of glass, mica and platinum. *J. Am. Chem. Soc*. 1917;40(9):1361-1403.
22. Erdogan FO. Freundlich, Langmuir, Temkin, DR and Harkins-Jura Isotherm studies on the adsorption of CO_2 on various porous adsorbents. *Int. J. Chem. React. Eng*. 2018;17: 221-234.
23. Ullah S, Bustam MA, Assiri MA, et al. Synthesis and characterization of mesoporous MOF UMCM-1 for CO_2/CH_4 adsorption; an experimental, isotherm modeling and thermodynamic study. *Micropor. Mesopor. Mater.* 2019;294:109844.
24. Hong DH, Suh MP. Enhancing CO_2 separation ability of a metal–organic framework by post-synthetic ligand exchange with flexible aliphatic carboxylates. *Chem. Eur. J.* 2014;20:426-434.
25. Poursaeidesfahani A, Andres-Garcia E, Lange M D, et al. Prediction of adsorption isotherms from breakthrough curves. *Micropor. Mesopor. Mater.* 2019;277:237-244.
26. Yasyerli S, Dogu G, Ar I, et el. Activities of copper oxide and Cu-V and Cu-Mo mixed oxides for H_2S removal in the presence and absence of hydrogen and predictions of a deactivation model. *Ind. Eng. Chem. Res.* 2001;40:1-9.
27. Kishor R, Ghoshal AK. APTES grafted ordered mesoporous silica KIT-6 for CO_2 adsorption. *Chem. Eng. J.* 2015;262:882-890.
28. Li B, Wen HM, Cui Y, et al. Emerging Multifunctional Metal-Organic Framework Materials. *Adv. Mater*. 2016;28: 8819-8860.
29. Zhang W, Lu J M, Liu Y, et al. Synthesis of metal organic framework UiO- 66 adsorbent by mixed ligands. *Mod. Chem. Ind.* 2019;396:107-119.
30. Gou PR, Hu SL. Hydrophobic modification of Ni-MOF-74 and its effect on CO adsorption performance. Atom *Energy Sci. Technol.* 2020;54:1192-1198.
31. Bao BZ, Yu L, Ren LQ, et al. Adsorption of CO_2 and CH_4 on a magnesium-based metal organic framework. *J.Colloid. Interface. Sci.* 2011;353:549-556.

32. Yang DA, Cho HY, Kim J, et al. CO_2 capture and conversion using Mg-MOF-74 prepared by a sonochemical method. *Energy Environ. Sci*. 2012;5:6465-6473.
33. Ammendola P, Raganati F, Chirone R, et al. Fixed bed adsorption as affected by thermodynamics and kinetics: yellow tuff for CO_2 capture. *Powder Technol*. 2020;373:446-458.
34. Raganati F, Chirone R, Ammendola P. Calcium-looping for thermochemical energy storage in concentrating solar power applications: Evaluation of the effect of acoustic perturbation on the fluidized bed carbonation. *Chem. Eng. J*. 2020;392:123658.
35. Cousin-Saint-Remi J, Stijn V, Segato T, et al. Highly robust MOF polymeric beads with controllable size for molecular separations. *ACS Appl. Mater. Inter*. 2019;11:13694-13703.